



Halogen-hydrogen bonds: A general synthetic approach for highly photoactive carbon nitride with tunable properties



Jesús Barrio^a, Andrea Grafmüller^b, Jonathan Tzadikov^a, Menny Shalom^{a,*}

^a Department of Chemistry and Ilse Katz Institute for Nanoscale Science and Technology, Ben-Gurion University of the Negev, Beer-Sheva 8410501, Israel

^b Department of Theory and Bio-Systems, Max Planck Institute of Colloids and Interfaces, Research Campus Golm, Potsdam 14424, Germany

ARTICLE INFO

Keywords:

Graphitic carbon nitride
Photocatalysis
Clean hydrogen production
Rational materials design
Hydrogen-halogen interaction
Supramolecular interaction

ABSTRACT

The design of the chemical, photo-physical, and catalytic properties of graphitic carbon nitride (g-CN) is highly challenging due to the harsh solid-state reaction. Here we report a template-free, large-scale synthesis of highly photoactive and stable g-CN with a unique dot-like morphology by using melamine-halogen complexes as starting precursor. The supramolecular structures are synthesized by sequential treatment of melamine with different acids. Experimental results together with theoretical calculations reveal that different halogens result in different interactions with melamine. We found that bromide reacts with the inner melamine aggregates while chloride is present mainly in the outer shell. Upon calcination, the delicate design results in porous carbon nitride with controlled morphologies and optical properties as well as improved charge separation under illumination and excellent photoactivity and stability for hydrogen production. Our results indicate that the type of halogen can significantly affect different properties in the final g-CN. This work provides new opportunities for template-free facile synthesis of highly photoactive carbon nitride and other carbon-nitrogen based materials with controllable chemical, optical, and catalytic properties for sustainable energy-related applications owing to the utilization of hydrogen-halogen based assemblies as well as the elucidation of their unique interaction.

1. Introduction

Graphitic carbon nitride (g-CN) is a metal-free semiconductor that has been extensively studied during the last decade [1–8] due to its outstanding electronic properties, which have been exploited in various applications, including photo- and electro-catalysis [9–11], for pollutants degradation [12,13], heterogeneous catalysis [14], CO₂ reduction [15], water splitting [16–19], light-emitting diodes [20], and solar cells [21]. The synthesis of g-CN comprises the thermal condensation of C- and N-rich monomers via a solid state reaction, which usually yields grain boundaries and unordered materials with low photo-catalytic activity. In the last years, many efforts have been made in order to modify the morphology, the electronic structure, and the catalytic properties of g-CN by using hard and soft templates [22], the introduction of heteroatoms [23,24], formation of heterojunctions with other materials [25–28], and exfoliation to thin layers [29]. Another successful approach to design and tune the morphology as well as the chemical, photophysical, and catalytic properties of CNs, is the supramolecular preorganization of C/N-based monomers, mainly based on hydrogen bonding, before calcination [30–36].

However, despite the significant progress in the synthesis of CNs,

the tailored design of properties already from the monomers level is still challenging due to the complexity of the solid-state reaction. The supramolecular approach allows a good control of the final CNs properties owing to the arrangement of the monomers prior the calcination. Up to date, mainly hydrogen bonds were used to manipulate the monomers due to their relative strength and abundant donor and acceptor sites on the monomers. Recently it has been shown that halogen-hydrogen interactions play a key role in the size and shape of aggregation of supramolecular complexes, providing a wide diversity of new chemical and photo-physical properties in g-CN upon calcination [37–42]. However, the effect and possibilities of these type of interactions are not fully understood. We report herein the synthesis of highly porous and photoactive carbon nitride by using supramolecular aggregates composed from melamine and different halogens. The starting supramolecular aggregates were carefully designed by a sequential treatment of the starting monomer with different halogenated acids. Experimental data and theoretical calculations are used to elucidate the interaction type of each halogen-acid and the monomer. Upon calcination, the starting composition determines the final photophysical, chemical, and catalytic properties of CN. The best CN exhibits very high specific surface area and 45 times higher hydrogen production rate under

* Corresponding author.

E-mail address: mennysh@bgu.ac.il (M. Shalom).

visible light compared to the pristine material.

2. Experimental section

2.1. Synthesis of catalysts

Supramolecular assemblies were prepared by soaking melamine (20 mmol) in aqueous solutions of HCl 37% (MC) and HBr 48% (MB) separately for 4 h using an automatic shaker and then centrifuged for 5 min at 6000 rpm. The resulting powders were soaked in an aqueous solution of the other halogen acid; MC in a solution of HBr 48% during 30 min, 4 h, and 8 h ($\text{MC}_{t(h)}$) and MB in a solution of HCl 37% ($\text{MBC}_{t(h)}$), for 4 h using an automatic shaker and then centrifuged for 5 min at 6000 rpm. The assemblies were dried at 60 °C in a vacuum oven overnight. Graphitic carbon nitride materials were prepared by calcining the assemblies at 500 °C for 4 h (heating rate of $2.3\text{ }^{\circ}\text{C min}^{-1}$) under nitrogen atmosphere ($\text{CN}_{t(h)}$, $\text{CNBC}_{t(h)}$). Reference CN was synthesized by heating up melamine to 500 °C for 4 h (heating rate of $2.3\text{ }^{\circ}\text{C min}^{-1}$) under an inert nitrogen atmosphere (CN).

2.2. Characterization

X-ray diffraction patterns were measured on an EMPYREAN instrument using Cu K α radiation. Nitrogen sorption measurements were taken using N₂ at 77 K after the samples had been degassed at 150 °C in vacuum for 20 h, using a Quantachrome Novatouch porosimeter. The apparent surface area of the final g-CN products was calculated by applying the Brunauer-Emmett-Teller (BET) model to the isotherm data points of the adsorption branch. Elemental analysis for CHNS was accomplished on Thermo Scientific Flash elemental analyzer OEA 2000. Scanning electron microscopy (SEM) and transmission electron microscopy (TEM) images were recorded using a JEOL JSM-7400 F high-resolution SEM operated at 3 kV and an FEI Tecnai T-12 TWIN TEM operated at 120 kV. FT-IR spectra were recorded on FTIR Spectrometer 6700. Optical absorbance spectra were measured on Cary 100 spectrophotometer equipped with an integrating sphere; fluorescence measurements were performed using a FLS920 P Spectrofluorimeter. XPS data were collected by using an X-ray photoelectron spectrometer ESCALAB 250 ultrahigh vacuum (1×10^{-9} bar) apparatus with an Al K α X-ray source and a monochromator. The X-ray beam size was 500 μm and survey spectra was recorded with a pass energy (PE) of 150 eV and high energy resolution spectra were recorded with a PE of 20 eV. To correct for charging effects, all spectra were calibrated relative to a carbon C 1 s peak, positioned at 284.8 eV. XPS results were processed by using the AVANTGE software. Mass-loss data of the functional groups were obtained in a Thermogravimetric Analyzer Q500. Hydrogen evolution measurements with 3 wt% Pt as a co-catalyst and triethanolamine (TEOA) as a hole-scavenger were performed using a schlenk flask thermostatically controlled with a cooling system and a white LED array as irradiation source. All catalytic experiments were conducted under an inert Ar atmosphere. In a H₂ evolution measurement, 15 mg of the sample were placed inside a 50 mL schlenk flask with the solvent mixture (19 mL), composed of water and TEOA in a 9:1 (v/v) ratio, and 19.6 μL of an 8% H₂PtCl₆ solution in water (corresponding to a theoretical value of 3 wt% Pt loading onto the catalyst, total concentration of 0.207 mM), the temperature was maintained at 25 °C with a thermostat. After being stirred for 30 min in the dark under constant Ar flow, the reaction started by switching on a 50 W (the illumination intensity on the photocatalyst surface was $10,000\text{ }\mu\text{mol s}^{-1}\text{ m}^{-2}$) white LED array (Bridgelux BXRA-50C5300; $\lambda > 410\text{ nm}$). In order to confirm that the evolved gas was hydrogen, the headspace of the reactor was analyzed by gas chromatography (Agilent 7820 GC System). Quantum yield measurements were performed in a sealed reactor connected to an argon line and an Agilent 7820 GC system. Argon gas was continually flowed through the reactor in the dark for removing the existing hydrogen, nitrogen, oxygen and other gases and

the purging process was monitored by automatically sampling every 11 min. [43]. After the purge, a Thorlabs LED (405 and 455 nm) was turned on, the hydrogen produced was recorded and the integrated area was used for the calculation of the average quantum yield (QY%) which was performed as follows: $\text{AQY} = \text{Ne}/\text{Np} \times 100\% = 2\text{ M}/\text{Np} \times 100\%$, where Ne is the amount of reaction electrons, Np is the incident photons, and M is the amount of H₂ molecules. The photocatalytic activity was further evaluated by the degradation of Rhodamine B (RhB) under white light irradiation. In a typical photocatalytic degradation experiment RhB (20 mL, 20 mg L⁻¹) and carbon nitride (20 mg) were mixed in a glass vial in the dark under continuous stirring until the adsorption-desorption equilibrium between the dye and the catalyst was obtained. After turning on the light, aliquots were withdrawn from the suspension at a given time interval. The concentration of the remaining RhB in solution was monitored by optical absorption (measured at $\lambda_{\text{max}} = 554\text{ nm}$). Electrochemical measurements were recorded using a three-electrode system on an Autolab potentiostat (Metrohm, PGSTAT 101). A Pt foil electrode and a Ag/AgCl (3 M KCl) electrode were used as the counter and reference electrode, respectively. Mott-Schottky ($1/\text{C}^2$ vs V) measurements were carried out in 1 M Na₂SO₄ aqueous solution as the electrolyte at a frequency of 2.48 kHz. Molecular Dynamics (MD) simulations were performed for melamine using force field parameters obtained from the ab database [44] for melamine and ion parameters from Reif and Hunenberger [45]. The simulation box contained 36 evenly distributed melamine molecules and 36 ions solvated with 650 SPCE water molecules. The systems were equilibrated for 2 ns using weak coupling [46], and then simulated for 100 ns with a 0.002 ps timestep at constant temperature of 300 K and constant pressure of 1 bar, controlled by the Nose-Hover Thermostat [47,48] and Parinello Rahman barostat [49], respectively, using the gromacs software [50]. Electrostatics were calculated using the particle mesh ewald method [51], bonds involving hydrogen atoms were constrained using LINCS [52] water molecules were kept rigid with SETTLE [53].

3. Results and discussion

The supramolecular assemblies were prepared by adding melamine to aqueous solutions of HCl (referred here as MC) and HBr (MB) separately. The assemblies were collected by centrifugation and the powders were isolated. Afterwards the MC and MB assemblies were added to the opposite halogen acid as shown in Fig. 1a (we refer here to the assemblies as MCB or MBC, where the B and C indicate each halogen acid).

Evidence of the formation of arrangements between melamine and the halogen acids is given by FT-IR spectroscopy and XRD analysis (Figs. 1, S1). The disappearance of the stretching and deformation bands of the amine groups (νNH_2) at $3469\text{--}3417\text{ cm}^{-1}$ and $1624\text{--}1648\text{ cm}^{-1}$ in all of the assemblies and a shift of the C–N stretching vibrations (νCN) to higher wavenumbers prove the interaction between melamine and the halogen acids. Furthermore, the treatment with a second halogen suppresses the ring breathing vibration of melamine at 810 cm^{-1} due to a more packed arrangement. P-XRD patterns of the assemblies show that bromine dominates the crystal structure. The repeating unit in plane at 9.8° in MC disappeared and the two new peaks emerged at 21.2° and 32° , correspond to a periodic alignment of melamine units along the (111) and (212) direction with $\pi\text{-}\pi$ interaction, owing to the Br interaction with melamine units [54]. The increasing amount of halogens in the supramolecular structures upon the addition of second halogen (Table S1), suggests that the second halogen does not only replace the first one but binds at other distinct sites. Due to the dominant role of Br in the MC assembly and the good photocatalytic performance of the corresponding carbon nitride (as will be shown later), we focus on the MCB system.

SEM images (Figs. 2 and S2) show similar morphologies for MC and MB assemblies, which consist of micrometer-long plate-like aggregates (Fig. S2a, b). After reaction of MC and MB with the second halogen,

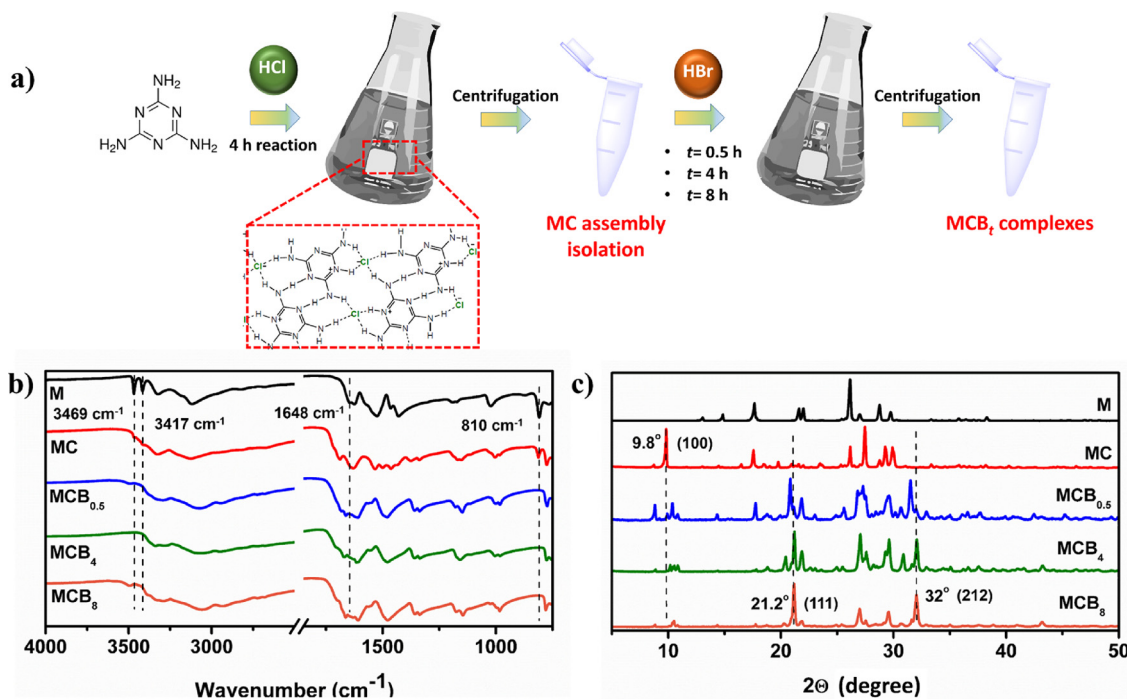


Fig. 1. a) Schematic synthetic route to MCB_t supramolecular assemblies, FT-IR spectra (b) and XRD (c) patterns of the different melamine-based assemblies.

different morphologies can be observed. MC displays flat plate-like assemblies (Fig. S2c), while Br addition to MC leads to the formation of long, layered, card-like aggregates. Fig. 2 shows that at longer HBr treatment the aggregate size was increased and an average aggregate size of more than 50 μm after 8 h treatment (Figs. 2, S3). Energy dispersive X-ray spectroscopy (EDS) analysis (Fig. S4) confirmed the presence of the two halogens in the different assemblies as well as the increase of Br wt% at longer treatments (up to 30 wt% after 8 h) and the decrease of Cl wt% (from 20% in the pristine MC assembly to 12% and 7% in $\text{MCB}_{0.5}$ and MCB_4 , respectively).

XPS analysis of the $\text{MCB}_{t(h)}$ assemblies was used to elucidate the elemental composition and chemical structure. MC and MB aggregates show the presence of Cl2p3 and Br3d5, respectively, and chemical states of N1 s prove their coordination with the melamine units (Fig. S5). N1 s spectra of MC and MB show four chemical species. Two of them belong to free amine groups (399.5 eV) and the C = N-C specie of triazine units (398.1 eV). The two remaining chemical species belong to the interaction of the amine groups in the melamine units with the halogen acids (396.9 eV in MC and 396.3 eV in MB), and to the coordination of HCl and HBr with the pyridinic N (395.1 eV in MC and

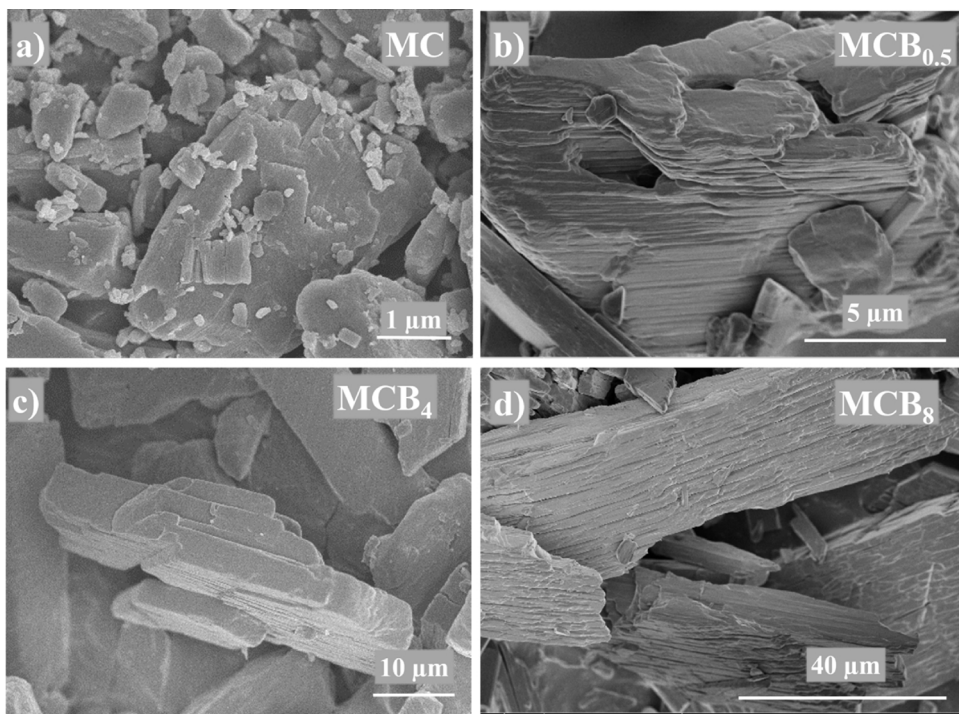


Fig. 2. SEM Images of the MC, MCB_t aggregates.

394.5 eV in MB) [55–57]. Cl2p3 and Br3d5 spectra for MC and MB, respectively, display two binding energies each that can be attributed to the interaction of the halogens with the amine groups (NH-X) and with the pyridinic nitrogens (N-X^-). In case of Cl2p3, at 196.6 (N-Cl) and 197.7 eV (NH-Cl), and for Br3d5 at 67.7 (N-Br) and 68.7 eV (NH-Br). We can observe that the contributions that belong to the interaction of halogens with the pyridinic nitrogen atoms possess a lower atomic weight percentage, (24% in Cl2p3 and 33% in Br3d5), suggesting that the interaction with the amine groups is more favorable than the coordination with the N in the melamine rings.

The insertion of HBr to MC suppresses the N-Cl contribution, meaning that Br substitutes Cl at the pyridinic sites and replaces part of the NH-Cl (Fig. S6). C1 s spectra of the assemblies show 3 different chemical states, at 284.8 eV (adventitious C–C bond), C–O contribution coming from adsorbed water at higher binding energies (286.8–287.5 eV), and the C = N-C at 288.8 eV. N1 s spectra display four binding energies in all the cases, corresponding to amine groups (399.5–400.0 eV), C = N-C from the triazine rings 398.5–398.8 eV, the interaction of amine groups with HCl and HBr (NH-X) at 396.8–397.4 eV, and the coordination of nitrogen in the melamine rings with Br, located at 395.4 eV.

The radial distribution functions of the halogens coordinating the amine groups and the pyridinic nitrogens are shown in Fig. 3a and b, respectively. Both clearly show stronger interaction with Br than with Cl. Comparing the distributions between the two sites, both ions coordinate the amine rather than the pyridinic nitrogen. During the course of the simulation, the 65–80 wt% of the Br ions are part of a melamine aggregate, whereas only 40–55 wt% of the Cl ions are incorporated in an aggregate. XRD patterns, XPS measurements and theoretical calculations prove that, due to a more feasible interaction of Br with the melamine units, the modifications imprinted by Br in the

MC supramolecular assembly are notably more significant than in the other way around (Cl in MB). As well, the final carbon nitride materials synthetized from MCB assemblies display beneficial characteristics for photocatalysis as we will show later in this manuscript. Therefore, this work will be focused in the MCB system and will try to elucidate the projection of a different morphology and chemical composition of a starting halogenated arrangement in the resulting C/N-based photoactive materials.

Photoactive graphitic carbon nitride materials were obtained by the thermal condensation of the prepared assemblies at 500 °C for 4 h under nitrogen. The condensation of the halogenated aggregates into carbon nitride materials was followed by TGA (Fig. S7), which shows that the halogen-melamine interaction strongly inhibits the melamine degradation and sublimation. The condensation of pure melamine to polymeric carbon nitride occurs mainly in one step with a weight loss of 85% around 380 °C. The insertion of HCl and HBr quenched melamine sublimation and the condensation process was split into several steps owing to the different polymerization path. The formation of CN materials was confirmed by FT-IR and XRD measurements (Figs. 4, S8). The stretching modes of CN heterocycles from 1200 to 1600 cm⁻¹ along with the breathing mode of the triazine units at 800 cm⁻¹ can be observed by FT-IR. The XRD patterns show the (100) and (200) crystal planes at around 13 and 27° typical of carbon nitride materials.

The morphology of the CN materials was altered according to the starting supramolecular assemblies as shown by SEM images (Figs. 5 and S9). The presence of HCl yields a porous framework (Fig. S9a) while the condensation of the MB produces a particle-like network with layered structures (Fig. S9b). The second halogen treatment of the starting supramolecular assembly leads to a morphological change of the final CNs. The effect on MCB species is shown in Fig. 5). After calcination, the outer part resembles the CN from MC (referred here as

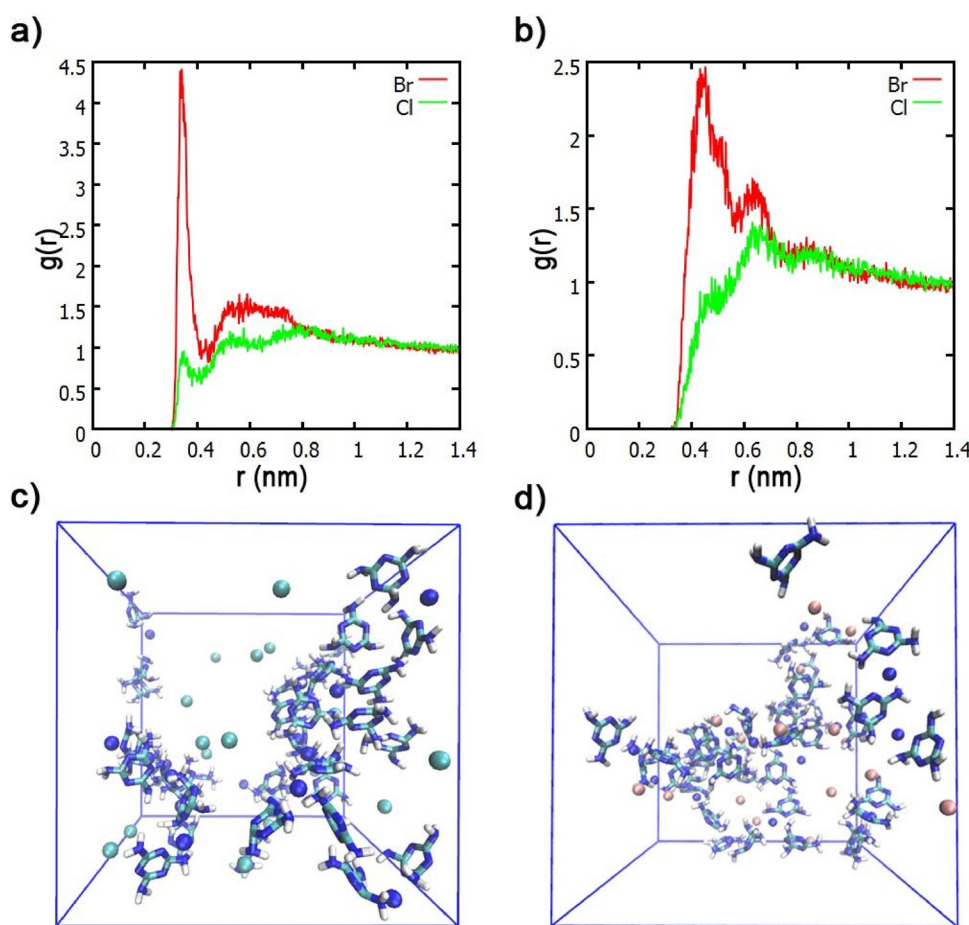


Fig. 3. Radial distribution function $g(r)$ around a) the amine and b) the pyridinic nitrogens measured in the MD simulations, and snapshots taken during the simulation with chlorine (c) and bromine (d). The colour scheme in the snapshots is the following: melamine molecules are drawn in stick representation with nitrogen in blue, carbon in cyan, and hydrogen in white. The ions are shown as van der Waals spheres in blue (Na^+), cyan (Cl^-), and pink (Br^-). The boxes are filled with water molecules which are not shown for clarity (For interpretation of the references to colour in this figure legend, the reader is referred to the web version of this article).

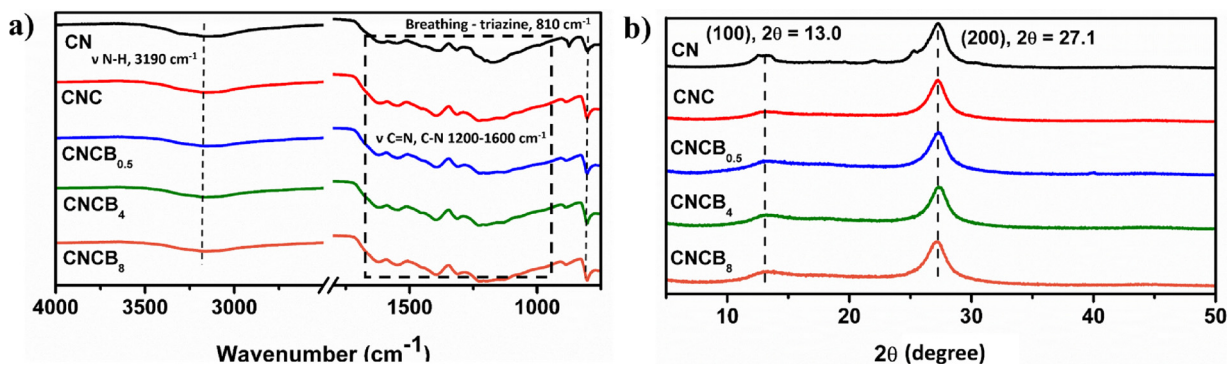


Fig. 4. FT-IR spectra (a) and XRD (b) patterns of CNCB materials.

CNC) while the inner part is similar to CN from MB (referred here as CNB), and a layered material with thick walls is obtained. On the other hand, a porous tube-like morphology was observed for the CN from MBC (referred here as CNBC) as shown in Fig. S9c. The layered structure of the materials was analyzed using TEM (Fig. S10); we envision that the increasing porosity of CNCB materials observed in the SEM images highly benefits the separation of the graphitic layers upon liquid exfoliation.

XPS analysis (Figs. 6, S11) further indicates the formation of CN materials and the absence of Cl or Br in the final structure after the thermal condensation. All the materials showed the characteristic binding energies of carbon nitride, C1 s spectra displays two different species corresponding to adventitious C–C (284.8 eV) and the C–N = C coordination (288.1 eV). N1 s spectra reveals several species corresponding to C–N = C coordination (398.5 eV), N-(C₃) (399.8 eV), remaining amino groups (NH₂, 401.2 eV), and a peak at higher binding energies which belongs to charging effects (404.2 eV).

The photophysical properties of the CN materials were optically characterized by UV-vis absorbance and photoluminescence (PL) spectroscopy (Fig. 7a–b). The new spatial arrangements in the MCB assemblies lead to a slight enhancement in the absorbance of the materials upon calcination. Furthermore, PL measurements show an important quenching of the main emission intensity, while the emission

related to the surface states remains unchanged, with longer times in the consecutive halogen treatments of the supramolecular assembly, which indicates an improvement in the charge separation of the excited charges. This fact could be due to formation of defects owing to halogen release upon condensation, leading to new non-radiative recombination pathways, which may be beneficial for photocatalysis.

To evaluate the photo-activity of the materials, we measured the RhB dye degradation as a function of time under white light illumination. Amongst all the materials, CNCB₈ showed the fastest photo-degradation performance (30 min), we note that RhB in the absence of catalyst didn't show any degradation (Figs. 7c, S12).

The mechanism of RhB degradation was elucidated by performing the experiment in the presence of a hole scavenger and an electron acceptor (TEOA and AgNO₃, respectively) and under Ar or O₂ environment (Fig. 7d). Purging the solution with Ar in order to remove dissolved oxygen, resulted in a decline of the photodegradation process, while the addition of 0.1 mL TEOA suppressed it completely. On the other hand, flushing with O₂ improved the photodegradation rates as well as the addition of 0.1 mL 0.1 M Ag⁺(aq). These results strongly suggest that the photochemical N-deethylation of RhB to the completely N-deethylated non-colored compound (rhodamine) occurs via oxidation by photogenerated holes.

Owing to its good photoactivity, the hydrogen production of CNCB₈

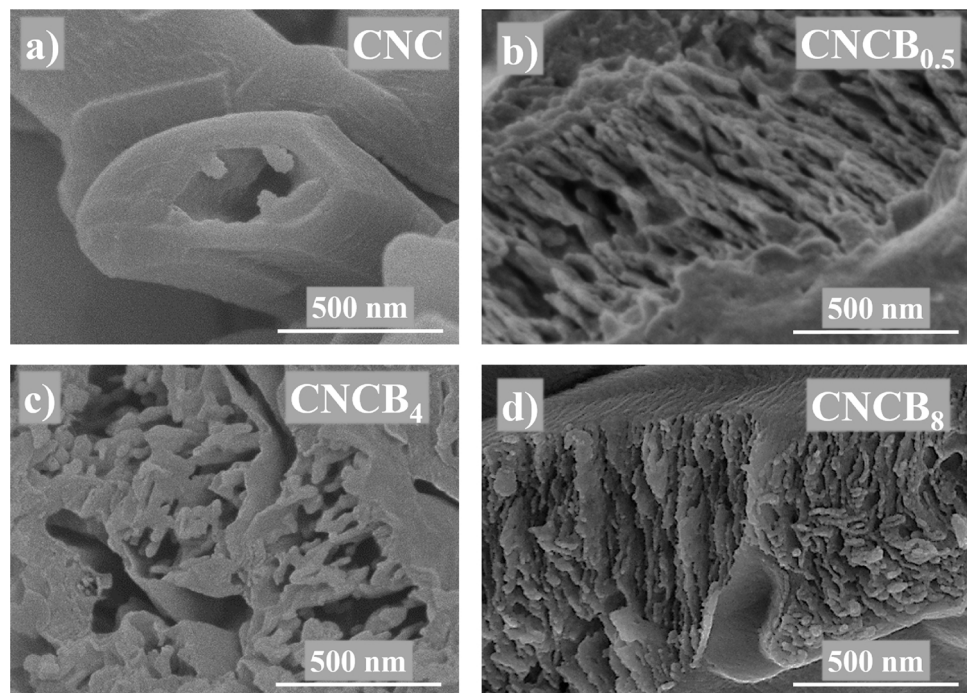


Fig. 5. SEM images of pristine CNC and CNCB_t materials.

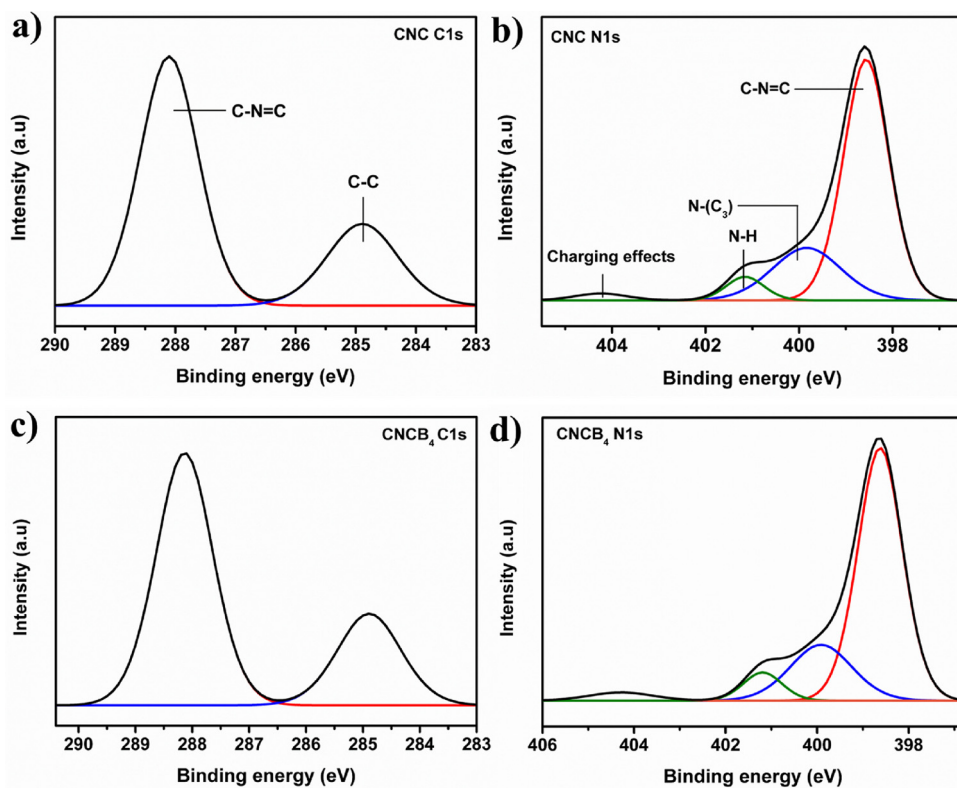


Fig. 6. XPS spectra for C1 s (a) and N1 s (b) of CNC and of CNCB_4 (c, d).

was measured in a water/triethanolamine (TEOA) solution, with Pt as the co-catalyst, under a white light illumination demonstrating 4 times higher catalytic activity compared to the pristine CN ($150 \mu\text{mol H}_2 \text{h}^{-1} \text{g}^{-1}$ vs $42 \mu\text{mol H}_2 \text{h}^{-1} \text{g}^{-1}$).

Recently, our group and others showed that the calcination of CN precursors to 650°C , can enhance the photocatalytic performance due to increased amount of defect sites and higher specific surface area [58–60]. Therefore, the MCB₈ was calcined at 650°C for 4 h under N_2

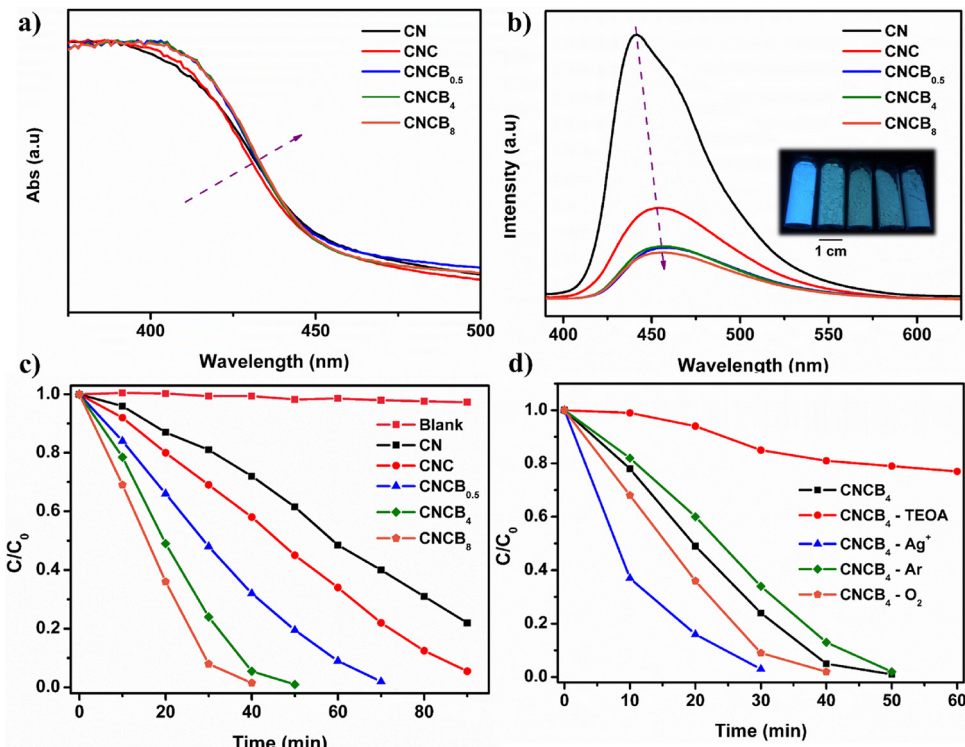


Fig. 7. (a) UV-vis diffuse reflectance and (b) PL emission spectra of CN materials. c) Photochemical degradation curves of RhB dye with CN materials and d) CNCB_4 with different additives. We note that the error bar is less than 2%.

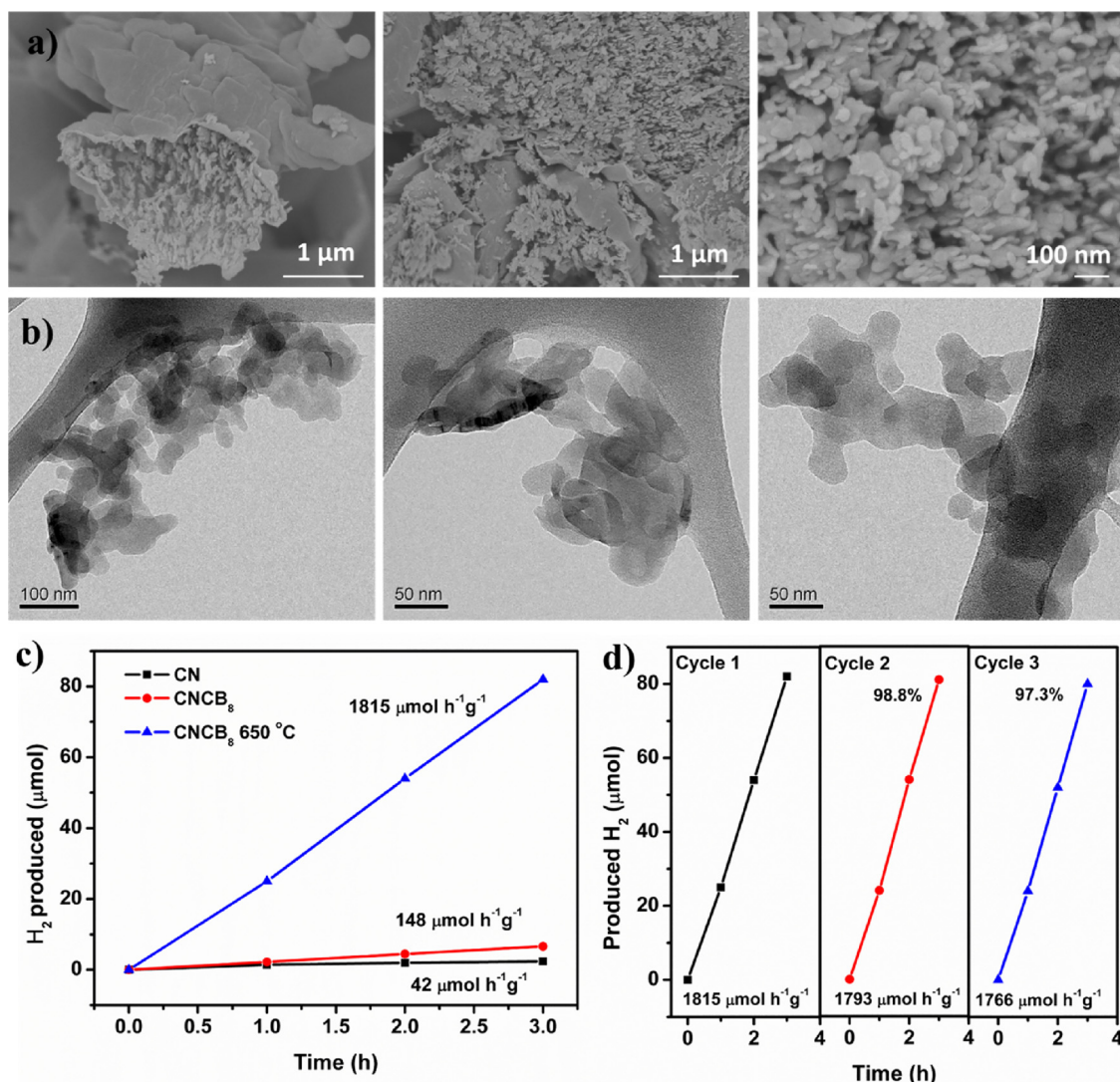


Fig. 8. (a) SEM, and (b)TEM images of CNCB₈ 650 °C, (c) H₂ evolution performance of CNCB₈ 650 °C under visible light, and (d) three consecutive cycles of H₂ evolution for the CNCB₈ 650 °C sample. We note that the error bar is less than 1%.

atmosphere. Elemental Analysis (EA, Table S2) demonstrates the formation of a better condensed polymeric carbon nitride material with less remaining N–H or NH₂ groups (the hydrogen wt% decreases in comparison to the CNCB materials calcined at 500 °C). FTIR spectra and XRD patterns (Fig. S13a–b) confirm that the structure still remains as a carbon nitride material, despite the high calcination temperature. The vibrations corresponding to the CN heterocycles between 1200–1600 cm^{−1} as well as the breathing mode of the triazine units at 800 cm^{−1} are visible in the FTIR spectra, while the XRD patterns show the peak corresponding to the (100) crystal plane at 13.0° and the (200), slightly shifted to 27.7° which corresponds to a *d*-spacing of 0.321 nm indicating a more compact carbon nitride [61]. The optical absorption of the CNCB₈ 650 °C reveals a new peak at 500 nm which can be attributed to increased amount of defects sites (Fig. S13c) [62–64]. The PL is further quenched compared to CNCB₈, which also indicates the formation of defects and better charge separation of the photo-excited states (Fig. S13d). XPS analysis (see Fig. S14 and discussion thereof) further demonstrated the formation of a carbon nitride-like material. SEM and TEM images (Fig. 8a, b) show the formation of a dots framework of an average size of 50 nm. BET measurements showed an enhancement in the specific surface area and pore volume of the material upon condensation at 650 °C compared to the assembly calcined at 500 °C ($70 \text{ m}^2 \text{ g}^{-1}$ and $0.36 \text{ cm}^3 \text{ g}^{-1}$ vs $20 \text{ m}^2 \text{ g}^{-1}$ and $0.06 \text{ cm}^3 \text{ g}^{-1}$,

Fig. S15). The photoactivity of the dots-like framework was analyzed by hydrogen production under white light (Fig. 8c) and this material showed remarkable hydrogen production values, 45-fold increase over the reference CN and 12-fold increase over the CNCB₈. The apparent QY (%) was measured at 405 and 455 nm, resulting in QY of 3.2% and 2.1% respectively. These values are relatively high considering that no doping or templating techniques were used. Importantly, the hydrogen production remained very stable during three subsequent catalytic cycles (Fig. 8d) and the characterization of the recycled material by FT-IR and XRD confirmed that the carbon nitride was undamaged (Fig. S16).

The enhanced photocatalytic activity could be due to several factors: better light harvesting leading to more charge carriers, better charge separation, and larger specific surface area providing higher amount of catalytic sites. With all data in hand we can see that, the described two-fold synthetic pathway induces a layered morphology, which leads to a higher specific surface area and results in the quenching of the PL owing to the creation of defects due to the release of Cl and Br. Both effects contribute to the enhancement of the photocatalytic activity. Furthermore, calcination to higher temperatures, produces an optimal morphology providing access to numerous catalytic sites. As well, the increased amount of defects at higher calcination temperatures modifies the electronic structure, and leads to enhancement of the optical absorption and an improvement in the charge

separation properties. Mott-Schottky measurements combined with Tauc plot indicate that the CN_{CB}₈ 650 °C conduction band is more negative compared to the reference carbon nitride (Fig. S17). We can conclude that all three factors contribute synergistically to a remarkable photoactivity in the hydrogen evolution reaction through water splitting under visible light and make the catalyst the most photoactive compared to the state-of-the-art materials synthetized in our group through different supramolecular structures (Table S3).

In summary, we demonstrated a facile, template-free synthesis of a highly photoactive carbon nitride-like dots framework by tailored design of supramolecular assembly that serves as the reaction precursor. The assemblies were acquired by a sequential treatment of melamine with two different halogenated acids. Theoretical and experimental data reveals that each halogen targets a different site in the starting precursor, leading to control over the final CN morphology, the specific surface area, and the photophysical and catalytic properties. In-depth characterization indicates that the most photoactive carbon nitride has more packed structure and high surface area as well as excellent catalytic activity owing to enhanced light harvesting properties and improved charge separation properties. The synergistic effect of the excellent photophysical properties, unique morphology, and high surface area leads to very high photocatalytic activity for hydrogen production with great stability during the course of measurement. We believe that this work opens new opportunities for the rational design of highly photoactive carbon nitride materials with a precise control over their chemical, photophysical, and catalytic properties beginning already at the monomers level.

Conflict of interest

The authors declare no conflict of interest.

Acknowledgements

The authors would like to thank Dr. Alexander Upcher and Dr. Einat Nativ-Roth from IKI for their assistance with electron microscopy, Dr. Guiming Peng for assistance with Mott-Schottky measurements, Mr. Eran Aronovitch for his help with QY measurements and Dr. Michael Volokh for fruitful discussion. This research was funded by the Israel Science Foundation (ISF), grant No. 1161/17.

Appendix A. Supplementary data

Supplementary material related to this article can be found, in the online version, at doi:<https://doi.org/10.1016/j.apcatb.2018.06.043>.

References

- [1] X. Wang, K. Maeda, A. Thomas, K. Takanabe, G. Xin, J.M. Carlsson, K. Domen, M. Antonietti, *Nat. Mater.* 8 (2009) 76–80.
- [2] W.J. Ong, L.L. Tan, Y.H. Ng, S.T. Yong, S.P. Chai, *Chem. Rev.* 116 (2016) 7159–7329.
- [3] J. Wen, J. Xie, X. Chen, X. Li, *Appl. Surf. Sci.* 391 (2017) 72–123.
- [4] J. Liu, H. Wang, M. Antonietti, *Chem. Soc. Rev.* 45 (2016) 2308–2326.
- [5] A. Thomas, A. Fischer, F. Goettmann, M. Antonietti, J.-O. Müller, R. Schlögl, J.M. Carlsson, *J. Mater. Chem.* 18 (2008) 4893.
- [6] J. Zhu, P. Xiao, H. Li, S.A. Carabineiro, *ACS Appl. Mater. Interfaces* 6 (2014) 16449–16465.
- [7] Y. Zheng, J. Liu, J. Liang, M. Jaroniec, S.Z. Qiao, *Energy Environ. Sci.* 5 (2012) 6717.
- [8] L. Chen, J. Song, *Adv. Funct. Mater.* (2017) 1702695.
- [9] S.C. Yan, Z.S. Li, Z.G. Zou, *Langmuir* 25 (2009) 10397–10401.
- [10] S. Yang, X. Feng, X. Wang, K. Müllen, *Angew. Chem. Int. Ed.* 50 (2011) 5339–5343.
- [11] M. Shalom, S. Gimenez, F. Schipper, I. Herranz-Cardona, J. Bisquert, M. Antonietti, *Angew. Chem. Int. Ed.* 53 (2014) 1–6.
- [12] J. Xu, T.J. Brenner, Z. Chen, D. Neher, M. Antonietti, M. Shalom, *ACS Appl. Mater. Interfaces* 6 (2014) 16481–16486.
- [13] J. Liu, T. Zhang, Z. Wang, G. Dawson, W. Chen, *J. Mater. Chem.* 21 (2011) 14398–14401.
- [14] J. Xu, L. Zhang, R. Shi, Y. Zhu, *J. Mater. Chem. A* 1 (2013) 14766.
- [15] J. Lin, Z. Pan, X. Wang, *ACS Sustainable Chem. Eng.* 2 (2014) 353–358.
- [16] X. Yang, H. Tang, J. Xu, M. Antonietti, M. Shalom, *ChemSusChem* 8 (2015) 1350–1358.
- [17] X. Wang, K. Maeda, X. Chen, K. Takanabe, K. Domen, Y. Hou, X. Fu, M. Antonietti, *J. Am. Chem. Soc.* 131 (2009) 1680–1681.
- [18] L. Lin, H. Ou, Y. Zhang, X. Wang, *ACS Catal.* 6 (2016) 3921–3931.
- [19] G. Zhang, Z.-A. Lan, L. Lin, S. Lin, X. Wang, *Chem. Sci.* 7 (2016) 3062–3066.
- [20] J. Xu, M. Shalom, F. Piersimoni, M. Antonietti, D. Neher, T.J.K. Brenner, *Adv. Opt. Mater.* 3 (2015) 913–917.
- [21] J. Xu, T.J.K. Brenner, L. Chabanne, D. Neher, M. Antonietti, M. Shalom, *J. Am. Chem. Soc.* 136 (2014) 13486–13489.
- [22] Z. Yang, Y. Zhang, Z. Schnepf, *J. Mater. Chem. A* 3 (2015) 14081–14092.
- [23] L. Jiang, X. Yuan, Y. Pan, J. Liang, G. Zeng, Z. Wu, H. Wang, *Appl. Catal. B* 217 (2017) 388–406.
- [24] C. Sun, H. Zhang, H. Liu, X. Zheng, W. Zou, L. Dong, L. Qi, *Appl. Catal. B: Environ.* 235 (2018) 66–74.
- [25] Y. Gong, X. Zhao, H. Zhang, B. Yang, K. Xiao, T. Guo, J. Zhang, H. Shao, Y. Wang, G. Yu, *Appl. Catal. B: Environ.* 233 (2018) 35–45.
- [26] D. Zeng, P. Wu, W.-J. Ong, B. Tang, M. Wu, H. Zheng, Y. Chen, D.-L. Peng, *Appl. Catal. B: Environ.* 233 (2018) 26–34.
- [27] Y. Wang, G. Tan, T. Liu, Y. Su, H. Ren, X. Zhang, A. Xia, L. Lv, Y. Liu, *Appl. Catal. B: Environ.* 234 (2018) 37–49.
- [28] W.-J. Ong, *Front. Mater.* 4 (2017) 11.
- [29] J. Ji, J. Wen, Y. Shen, Y. Lv, Y. Chen, S. Liu, H. Ma, Y. Zhang, *J. Am. Chem. Soc.* 139 (2017) 11698–11701.
- [30] M. Shalom, S. Inal, C. Fettkenhauer, D. Neher, M. Antonietti, *J. Am. Chem. Soc.* 135 (2013) 7118–7121.
- [31] Y.-S. Jun, E.Z. Lee, X. Wang, W.H. Hong, G.D. Stucky, A. Thomas, *Adv. Funct. Mater.* 23 (2013) 3661–3667.
- [32] J. Sun, J. Xu, A. Grafmueller, X. Huang, C. Liedel, G. Algara-Siller, M. Willinger, C. Yang, Y. Fu, X. Wang, M. Shalom, *Appl. Catal. B* 205 (2017) 1–10.
- [33] L.-L. Feng, Y. Zou, C. Li, S. Gao, L.-J. Zhou, Q. Sun, M. Fan, H. Wang, D. Wang, G.-D. Li, X. Zou, *Int. J. Hydrogen Energy* 39 (2014) 15373–15379.
- [34] G. Peng, L. Xing, J. Barrio, M. Volokh, M. Shalom, *Angew. Chem. Int. Ed.* 57 (2018) 1186–1192.
- [35] Y. Liao, S. Zhu, J. Ma, Z. Sun, C. Yin, C. Zhu, X. Lou, D. Zhang, *ChemCatChem* 6 (2014) 3419–3425.
- [36] M. Shalom, M. Guttentag, C. Fettkenhauer, S. Inal, D. Neher, A. Llobet, M. Antonietti, *Chem. Mater.* 26 (2014) 5812–5818.
- [37] J. Barrio, M. Shalom, *Mat. Sci. Semicond. Process.* 73 (2018) 78–82.
- [38] Y. Hong, C. Li, D. Li, Z. Fang, B. Luo, X. Yan, H. Shen, B. Mao, W. Shi, *Nanoscale* 9 (2017) 14103–14110.
- [39] M. Xie, W. Wei, Z. Jiang, Y. Xu, J. Xie, *Ceram. Int.* 42 (2016) 4158–4170.
- [40] L. Li, M. Shalom, Y. Zhao, J. Barrio, M. Antonietti, *J. Mater. Chem. A* 5 (2017) 18502–18508.
- [41] G. Dong, L. Zhang, *J. Mater. Chem.* 22 (2012) 1160–1166.
- [42] J. Barrio, L. Lin, X. Wang, M. Shalom, *ACS Sustainable Chem. Eng.* 6 (2018) 519–530.
- [43] P. Kalisman, Y. Nakibli, L. Amirav, *Nano Lett.* 16 (2016) 1776–1781.
- [44] A.K. Malde, L. Zuo, M. Breeze, M. Stroet, D. Pogar, P.C. Nair, C. Oostenbrink, A.E. Mark, *J. Chem. Theory Comput.* 7 (2011) 4026–4037.
- [45] M.M. Reif, P.H. Hünenberger, *J. Chem. Phys.* 134 (2011) 144104.
- [46] H.J. Berendsen, J.v. Postma, W.F. van Gunsteren, A. DiNola, J. Haak, *J. Chem. Phys.* 81 (1984) 3684–3690.
- [47] W.G. Hoover, *Phys. Rev. A* 31 (1985) 1695.
- [48] S. Nosé, *J. Chem. Phys.* 81 (1984) 511–519.
- [49] M. Parrinello, A. Rahman, *J. Appl. Phys.* 52 (1981) 7182–7190.
- [50] D. Van Der Spoel, E. Lindahl, B. Hess, G. Groenhof, A.E. Mark, H.J. Berendsen, *J. Comput. Chem.* 26 (2005) 1701–1718.
- [51] T. Darden, D. York, L. Pedersen, *J. Chem. Phys.* 98 (1993) 10089–10092.
- [52] B. Hess, H. Bekker, H.J. Berendsen, J.G. Fraaije, *J. Comput. Chem.* 18 (1997) 1463–1472.
- [53] S. Miyamoto, P.A. Kollman, *J. Comput. Chem.* 13 (1992) 952–962.
- [54] R.S. Bhosale, M. Al Kobaisi, S.V. Bhosale, S. Bhargava, S.V. Bhosale, *Sci. Rep.* 5 (2015) 14609.
- [55] L. González, N. Gimeno, R.M. Tejedor, V. Polo, M.B. Ros, S. Uriel, J.L. Serrano, *Chem. Mater.* 25 (2013) 4503–4510.
- [56] B. Roy, P. Bairi, A.K. Nandi, *RSC Adv.* 4 (2014) 1708–1734.
- [57] J. Xu, G. Wu, Z. Wang, X. Zhang, *Chem. Sci.* 3 (2012) 3227.
- [58] B. Jesús, L. Lihua, A.O. Pilar, T. Jonathan, P. Guiming, S. Jingwen, Z. Félix, W. Xinchen, S. Menny, *Small* 14 (2018) 1800633.
- [59] P. Niu, M. Qiao, Y. Li, L. Huang, T. Zhai, *Nano Energy* 44 (2018) 73–81.
- [60] J. Xu, Y. Li, S. Peng, G. Lu, S. Li, *Phys. Chem. Chem. Phys.* 15 (2013) 7657–7665.
- [61] G. Zhang, J. Zhang, M. Zhang, X. Wang, *J. Mater. Chem.* 22 (2012) 8083–8091.
- [62] T. Jordan, N. Fechner, J. Xu, T.J.K. Brenner, M. Antonietti, M. Shalom, *ChemCatChem* 7 (2015) 2826–2830.
- [63] W. Tu, Y. Xu, J. Wang, B. Zhang, T. Zhou, S. Yin, S. Wu, C. Li, Y. Huang, Y. Zhou, Z. Zou, J. Robertson, M. Kraft, R. Xu, *ACS Sustainable Chem. Eng.* 5 (2017) 7260–7268.
- [64] P. Niu, G. Liu, H.-M. Cheng, *J. Phys. Chem. C* 116 (2012) 11013–11018.